Quantitative PEEM and Raman study of nanorough Au SERS-Active substrates for molecular sensing applications

Pierre Taugeron, Meryem Rahmani, Nicolas Delorme, Mathilde Faure, Ludovic Douillard, Jean-François Bardeau

Performance of metal SERS-active substrates: A quantitative PEEM and Raman study

Pierre Taugeron[†], Meryem Rahmani[†], Nicolas Delorme[†], Mathilde Faure[‡], Ludovic Douillard[‡], Jean-François Bardeau[†*]

[†] Institut des Molécules et Matériaux du Mans CNRS 6283, Le Mans Université, F-72085 Le Mans, France

[‡] Université Paris-Saclay, CEA SPEC, CNRS 3680, F-91190 Gif-sur-Yvette, France

KEYWORDS

Nanorough metallic surface; Plasmonics; Photoemission electron microscopy; Surface-Enhanced Raman Scattering SERS

ABSTRACT

Surface-enhanced Raman Scattering (SERS) is a well-established surface-sensitive technique for detecting the presence of trace amounts of molecular analytes. While the impact of surface singularities on plasmonic materials has been widely studied, fabrication of cost-effective efficient SERS substrates remains a challenge. In this paper, we present the study of large area Au SERS-active substrates, elaborated by thermal evaporation deposition, by photoemission electron microscopy (PEEM), a high-resolution near-field mapping technique, to access the statistical properties of the hot spot distribution. We experimentally demonstrate that the near field PEEM and far field Raman statistical signatures of nanorough Au surfaces are quantitatively correlated when used for molecular sensing. The maximum of the SERS signal of thiophenol (TP) molecules diluted to 10^{-6} M is observed near the film percolation threshold for which the hot spot density is maximum. Finally, SERS measurements from solutions of thiophenol (TP), Crystal Violet (CV)

and rhodamine B (RhB) molecules at 10^{-8} M demonstrated the sensitivity of our substrates for molecular sensing.

INTRODUCTION

Surface Enhanced Raman Spectroscopy (SERS), discovered in the 1970s[1], is a well-known non-invasive, ultra-sensitive label-free tool for detection, identification and quantification of materials and molecular analytes.[1–4]. It is now commonly accepted that SERS phenomenon is based on two major mechanisms.[4,5] First, a chemical effect is invoked when the polarizability of the analyte molecule is modulated as a result of a charge transfer mechanism between a substrate and the target molecule.[4,6] Second and largest contribution for the enhancement factor is due to an electromagnetic mechanism.[4,7] Strong Raman signal enhancements can be observed when the energy of the laser excitation is close to the surface plasmon energy of a metallic substrate. Indeed, under optical excitation, and at certain wavelengths, a random metal surface is the site of coherent charge oscillations, called *localized surface plasmons* (LSP)[7]. LSP generate greatly enhanced electromagnetic fields confined to nanoscale regions. In particular, huge enhancements of the induced electromagnetic field can be observed at locations where narrow gaps between nanoparticles (NPs) or surface heterogeneities[8] exist; these sites are called "hotspots".

Given its sensitivity to detect the presence of very low dose of analytes in solution down to a single molecule[9], the SERS method still attracts as much attention from the research communities on the fundamental and applied research aspects. Over the last decade, several strategies have emerged to prepare efficient, uniform and large SERS substrates. In particular, those employing solutions of colloidal nanoparticles are common as it is certainly the most cost-effective way to develop solid SERS substrates. However, it is quite difficult to control the topographic properties of the substrate on a large scale from one manufacturer to another, due to the inhomogeneity of the

particle size and shape distributions, resulting in large variations in the Raman signal. These disadvantages have not prevented this technique from being widely applied in many applications.[10,11]

So, one of the greatest challenges for the quantitative use of SERS remains the reproducible design and fabrication of substrates with topographic features of high enhancement factors and hot spot density on a large scale. Complex and/or expensive fabrication methods such as electron beam lithography[12–15], or ion-beam lithography [16,17] are increasingly used to develop small areas, of precisely controlled geometries and/or periodic arrangements of plasmonic nanostructures. An alternative simple method for preparing a SERS substrate is the physical vapor deposition (PVD) including thermal evaporation, sputtering and electron beam evaporation.[18–22] Thin films of noble metals deposited by PVD process usually form on smooth surfaces, for reasons of poor wetting and low surface energy, isolated particulate nanostructures. The distance between these particles can then be reduced to dimensions below one nm, which is particularly well suited to plasmonic activities.[23,24]

Many experimental parameters, such as deposition rate, substrate temperature, vacuum pressure and nominal deposited film thickness can influence the resulting surface morphology. Indeed, the chemical nature of the support can influence the organization of the metal deposited on the surface as well as various post-deposition treatments such as thermal annealing, solvent annealing, or chemical functionalization. Beyond a certain thickness threshold which can vary from ~20 to 50 nm, the metallic film becomes entirely continuous[25,26], has an optical mirror appearance, and the plasmonic activity is considerably reduced. Nevertheless, the literature reports SERS effects for films with nominal thicknesses between 0.1 and 4 µm[26,27] at the cost of a *reduced detection limit*

(LOD) of the analyte, i.e. detectable concentrations ranging from 10^{-3} to 10^{-6} M for molecules such as Rhodamine 6G, Methylene blue or Cysteamine.

Considering the role played by the nanoscale film topography in Raman enhancement, it is important to better understand how the SERS intensity correlates with both the surface density and the intensity distribution of the hot spots. PEEM microscopy is a powerful and non-intrusive near-field mapping technique with a minimum spatial resolution of 10 - 20 nm [28–30]. This technique may therefore be particularly useful in studying the Raman scattering physics at a scale below the diffraction limit near the film percolation threshold. The PEEM imaging principle is based on the collection of electrons emitted from a surface, regardless of the mechanism involved: thermoionic, photoelectric,... In the irradiance range of SERS, near-field plasmonic enhancements lead to strong modulations of the photoelectric effect, the electron emission regime becomes multiphotonic in nature, and the recorded intensities follow a nonlinear scaling law in incident electric field E^{2n} (n *photon photoemission signal* nPPE). For Au material the PEEM signal corresponds to a three photon absorption event. The PEEM technique provides very contrasted images in intensity reflecting the distribution of the hot spots on the sample surface at a sub-wavelength scale.

In the present paper, we propose to quantitatively study the correlation of the optical responses of SERS substrates at different scales, in particular, from the optical near-field description as measured by PEEM to its far-field counterpart as measured by Raman. With this objective, it is of particular interest to study how the surface density and intensity distributions of the film hot spots determine quantitatively the resulting Raman signal when molecules are grafted on the surface. Our investigations will be carry out on a series of Au substrates fabricated by thermal evaporation in order to optimize and validate the experimental fabrication conditions. For Raman studies our substrates are at first functionalized with thiophenol (TP) molecules, as model molecules, as they

bind easily to any Au surface (with its thiol function) to form an homogenous monolayer after rinsing[27]. Finally, the overall sensing performance of our optimized substrates are tested and discussed with solutions of thiophenol (TP), Crystal Violet (CV) and Rhodamine B (RhB) molecules at 10^{-8} M.

RESULTS AND DISCUSSIONS

The substrates were prepared following the procedure described in Scheme 1 in Experimental Section. In order to directly observe the effect of an additional Au layer on the surface morphologies, SEM images have been recorded (Figure 1) for different exposure times (surface coverage). Note that the "0 s" substrate is the reference sample and corresponds to a pristine 100 nm thick Au layer. As expected, the gold surface of the reference sample is not flat but exhibits spherical clusters/rounded gold mounds with relatively uniform dimensions. The lateral diameters of the metal clusters are in the 15 – 20 nm range with a maximum in the height distribution around 16 nm. These surface protrusions are separated from each other by distances of the same order of magnitude. Such topographies have already been reported for gold deposited on silica and mica[31–33]. For these cases, the non-wetting nature of gold on the oxide substrate promotes the coalescence of grains into clusters. The growth mechanism of metal layers mainly depends of both the respective surface tensions at the interfaces crystallite–substrate, crystallite–gold vapor, and substrate–gold vapor. During the thermal evaporation process, the Au adatoms, once deposited on the surface, diffuse slowly on the surface, form nucleii at random locations on the surface and evolve as charged nano-sized clusters. The presence of charge plays an important role in maintaining on surface clusters even if the substrates are made of the same metal. For increasing

exposure times, the density of adatoms increases, which increases the phenomenon of nucleation and the interactions between clusters. Using statistical methods such as the one developed in our group[34], it is possible to analyze the SEM images and determine the average grain size as function of the deposition conditions. Table 1 reports the quantitative evolution of the average surface grain size, determined by interface distribution function (IDF) method. Grain size is essentially independent of exposure time, a significant increase of the grain diameter is only observed for a deposition time of 150s.

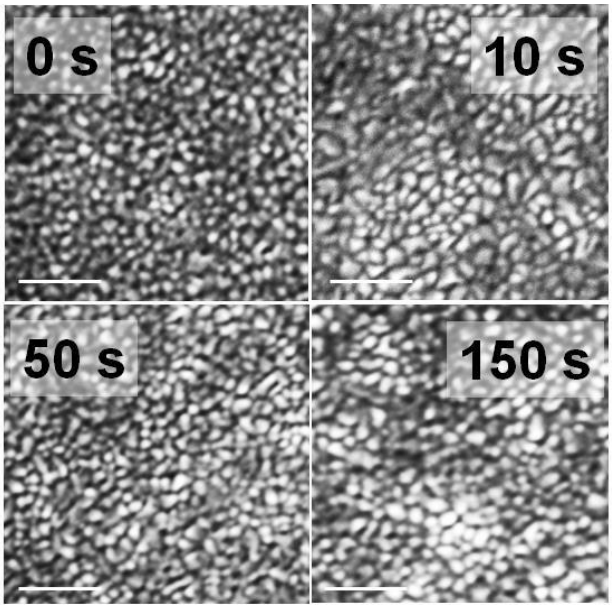

Figure 1. SEM images of Au surfaces after additional Au layer deposition for different exposure times, respectively. The white scale bar is 200 nm.

Deposit duration (s)	Gold layer thickness H (nm)	Average grain diameter (nm)	Coverage rate	Intergrain distance on simulated surfaces (nm)
0	0	30.8 ±0.4	0.52	8.1 ±0.2
10	1±0.2	31.4 ±0.5	0.54	8.1 ±0.2
50	8.2±0.2	30.6 ±0.4	0.64	3.9 ±0.2
70	11.4±0.2	33.2 ±0.4	0.69	4.3 ±0.2
150	19.5±0.2	36.6 ±0.4	0.78	4.8 ±0.2

Table 1. Au film metrology. Evolution of gold layer thickness, the mean surface grain diameter and surface coverage as calculated using the interface distribution function (IDF) method versus the gold deposition time. The intergrain distance is estimated using the IDF method on simulated surfaces made of nanodisks with controlled surface coverage and diameter.

Due to the small intergrain distances (< 10 nm), the resolution of the SEM images is not high enough to allow their determination. However, during the growth process, the coverage of the metal increases on the surface, the clusters of metal connect to each other to first create irregular shapes with small asperities before forming a continuous film over time [26,35–37]. In the theory of continuous

two-dimensional percolation [38,39], statistical physics shows a direct analytical link between the percolation threshold and the surface coverage. In the case of disc percolation, the numerical estimate of the percolation threshold corresponds to a surface coverage of 0.676. The surface coverage measurements reported in Table 1 show that the Au film closest to the percolation threshold corresponds to a deposition time between 50 and 70 s, i.e. between 8.2 and 11.4 nm of gold layer thickness as determined by atomic force microscopy (AFM) (see experimental part).

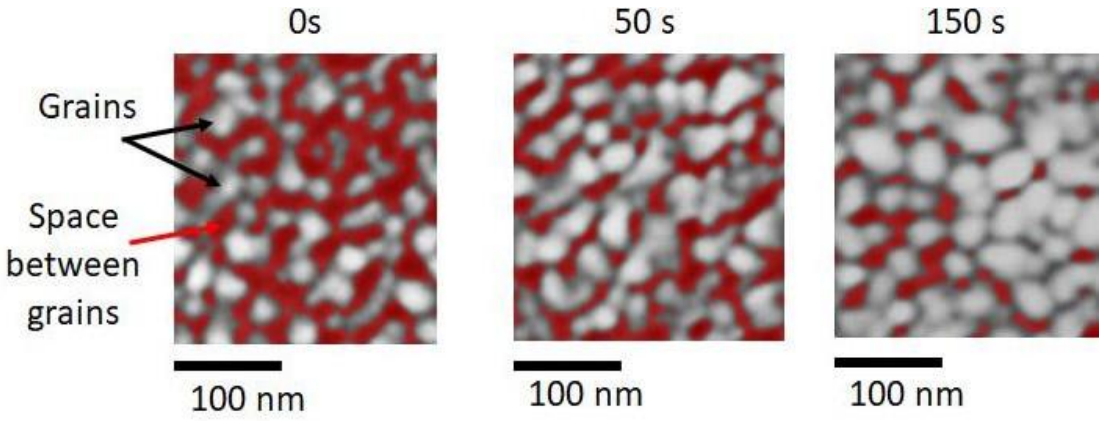

Figure 2: SEM images of Au surfaces with a colored mask (threshold value = 40% of the maximum height) revealing the decreasing of the intergrain areas versus the gold deposition time. Percolation threshold corresponds to image 50s i.e. an additional Au film deposit of 8.2 nm in thickness.

Alternatively, by extracting 300 x 300 nm² area from the SEM images and by performing a height-threshold masking (i.e. threshold value = 40% of the maximum height) the intergrain regions can be visualized (Figure 2). From these images we can observed a decrease with the deposition time of the intergrain area (colored part of the mask). From t = 50 s random individual grains start to enter in contact with neighboring grains to form a long-range connectivity network. The occurrence of a long-range connectivity within the metal deposit defines the percolation threshold. From our results thickness of 8.2 (±0.2) nm is expected for percolation threshold [40,41].

On the other hand, we can also create a model surface (Figure S1) made of nanodisks regularly dispersed on a surface respecting the values of coverage rate and grain diameter (Table 1) to estimate the distance between the nanoobjects. The calculated values (Figure S1), presented in the last column of Table 1, show that the lowest distance is obtained when the deposition time is 50 s. The intergrain distances are obviously overestimated in this approach but this result confirms therefore that the percolation threshold is obtained for deposition times of 50 s, i.e. 8.2 (±0.2) nm.

In the following we deposited gold layer of about 1(±0.2), 8.2(±0.2) and 19.5(±0.2) nm on 100 nm Au/Si substrate in order to investigate the optical near-field responses of the nanorough Au surfaces. Figure 3 shows the optical near-field responses of the different Au substrates as a function of the thickness of the deposited gold layer as determined by PEEM microscopy. The resolution of the instrument and the non-linear three-photon absorption process make it possible to obtain very contrasted images (the noise signal being limited) on which it is easy to discern and therefore count the hot spots by image processing (cross correlation procedure, see experimental part). Let us note that the PEEM resolution is directly related to the optical near field distribution and not to the size of the excitation beam (full field excitation). It is clear that the reference sample (0 nm) and the sample with 1 nm of gold have less than ten low intensity hot spots on a surface of 315 µm² (pi x 10 µm²). In contrast, the two other samples generate much more hot spots, homogeneously (at the micron scale) distributed over the surface.

Analysis of the averaged PEEM signal intensity per µm² for each substrate (calculated from the sum of the intensities of all the hotspots divided by their number on a reference area) is also very informative (Figure 4). The surface density of hot spots per µm² is shown for the series of substrates in Figure S2. Hot spot surface density varies with surface preparation conditions and the highest

density of hot spots is achieved for the 8.2 nm coated sample with a value of 15 detectable hot spots / µm².

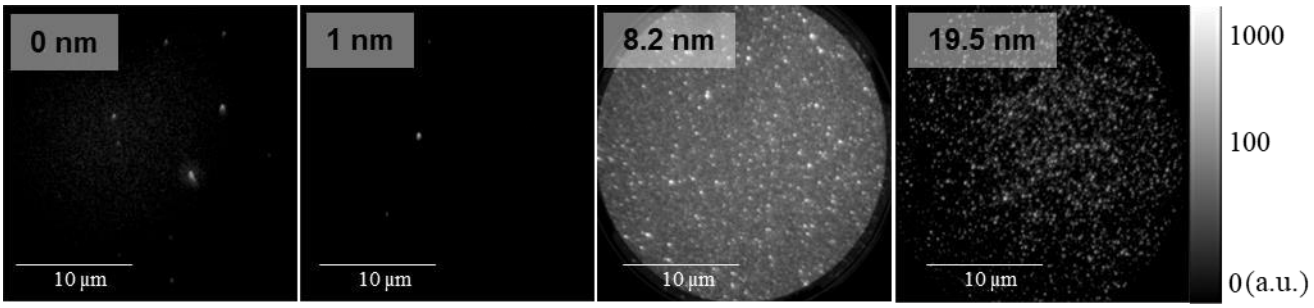

Figure 3. 3PPE PEEM images (25 x 25 µm^2) of 0, 1.0, 8.2 and 19.5 nm gold layer deposited on 100 nm Au/Si substrate. PEEM intensities are normalized and displayed on a log scale. Laser wavelength λ = 633 nm, laser irradiance 2 GW/ cm², p-polarization under grazing incidence, acquisition time t = 1 s.

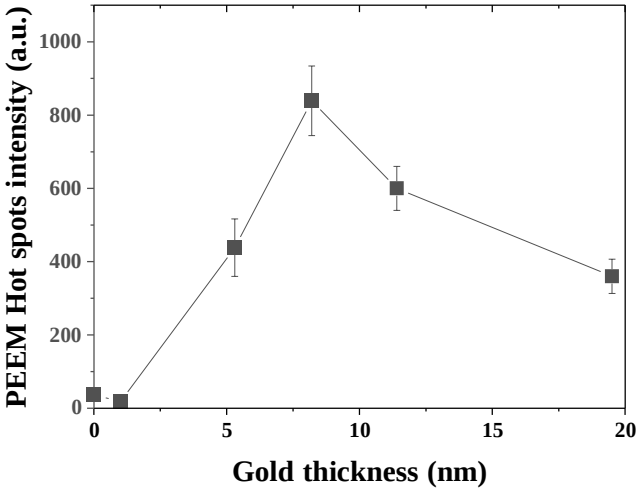

Figure 4. Averaged 3PPE PEEM Hot spot intensity per µm² as function of the thickness of the deposited gold layer. Laser wavelength λ = 633 nm, laser irradiance P = 2 GW / cm², P polarization under grazing incidence.

The results shown in Figure 4 and Figure S2 provide a rough estimate of the plasmonic contribution to the SERS signal exaltation. Indeed, these results unambiguously confirm that the 8.2 nm coated

sample is the most efficient plasmonic substrate in our series and that the highest hot spot density is reached at the film percolation threshold where the intergrain distance is the smallest[42]. To go further, a quantitative determination of field enhancement factors remains a difficult problem. A possible way is to exploit the evolution of the cut-off energy of the electron kinetic energy distribution curve at the transition between a nonlinear photoelectric regime and a field emission regime. Following P. Rácz et al. [43], we determined the average enhancement factor on the 8.2 nm Au coated film to 29^6. This field enhancement factor represents an average of the maximum factors at the scale of a 1 µm region. It quantifies an upper limit of the electromagnetic contribution of the SERS phenomenon.

Accordingly, we have demonstrated that very slight modifications of the substrate processing conditions, generating topographic modifications at the nanoscale that are difficult to quantify, can generate quite significant changes in terms of hot spot density and plasmonic activity. However, the experimental process used to fabricate the samples is sufficiently reproducible to be able to repeat several series of samples and confirm our experimental results as shown in Figure 4. This is a key advantage as we want to optimize our substrates for trace molecule detection.

In parallel to near field responses, far field SERS efficiencies of our substrates are determined. To do this, the surfaces were functionalized by a 10^{-6} M thiophenol solution in ethanol. The treatment is identical for all the samples of the series. After functionalization of the surfaces, 400 spectra were recorded from a 20 x 20 µm² area mapping with a 2D map step size of 1 µm. For each substrate, three maps were systematically recorded on different areas and two series of samples have been studied. Figure 5A highlights normalized Raman intensity mapping on the series of substrates; note that the 8.2 nm coated surface generates higher Raman intensities. Figure 5B shows the averaged spectra of an intensity Raman mapping for each film deposition time. It is clear that

the film growth conditions strongly influence the enhancement factors observed in Raman. The intensity of the average Raman mapping spectrum reaches a maximum for the 8.2 nm coated substrate. This result is in good agreement with PEEM results and the increase in hot spot density.

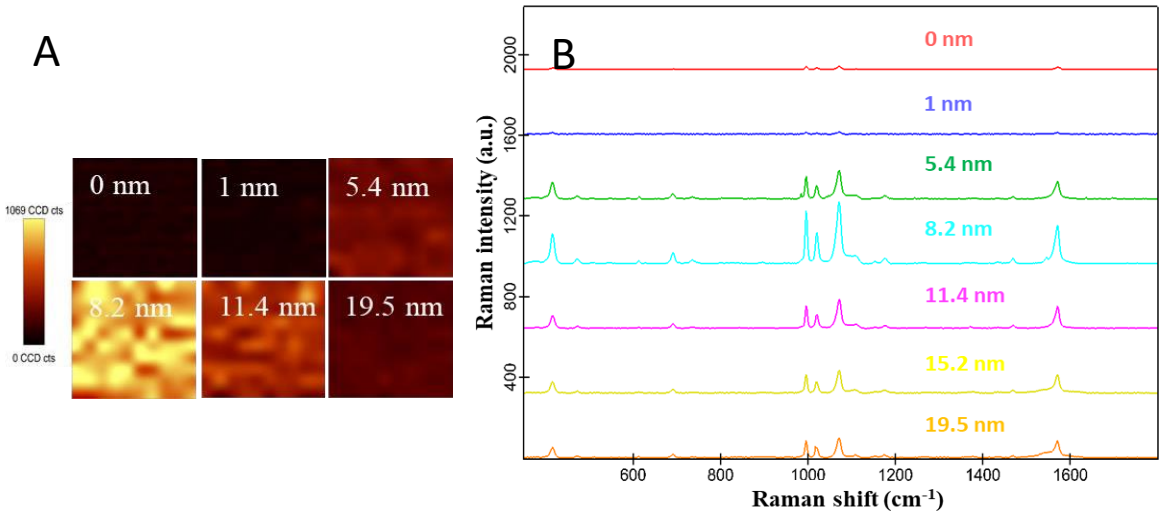

Figure 5. Raman measures. A) Examples of normalized Raman intensity maps of thiophenol at 10^{-6}M based on 400 spectra recorded in 20 x 20 µm² area. P= 2 mW; t= 0.5s; λ=633 nm. The intensity of the Raman spectrum is calculated in the range 300 - 1800 cm^{-1}, B) Averaged Raman spectra calculated from the recorded maps i.e. for different gold layer thickness (0, 1, 5.4, 8.2, 11.4, 15.2 and 19.5 nm). The Raman spectra are vertically shifted for clarity.

Figure 6 shows the averaged integrated Raman intensity (based on 400 spectra recorded in 20x20 area µm² area) for the series of substrates in the wavenumber range 300-1800 cm^{-1}. If we compare the Raman intensity values for each substrate to the one obtained when the Au substrate was not coated by a second gold layer, we obtain the multiplicative factor of the second axis. Figure 6 shows a strong increase in intensity from 0 to 8.2 nm and a slower decrease thereafter, in agreement with the PEEM results (shown in Figure 4). The relative standard deviation (RSD) values of the calculated Raman intensities in the range 300-1800 cm-1 over 2 sets of samples and three maps

(recorded on each substrate) is about 3%. Such a result prove that the thermal evaporation process allows to obtain homogeneous surfaces on large areas with a high reproducibility rate.

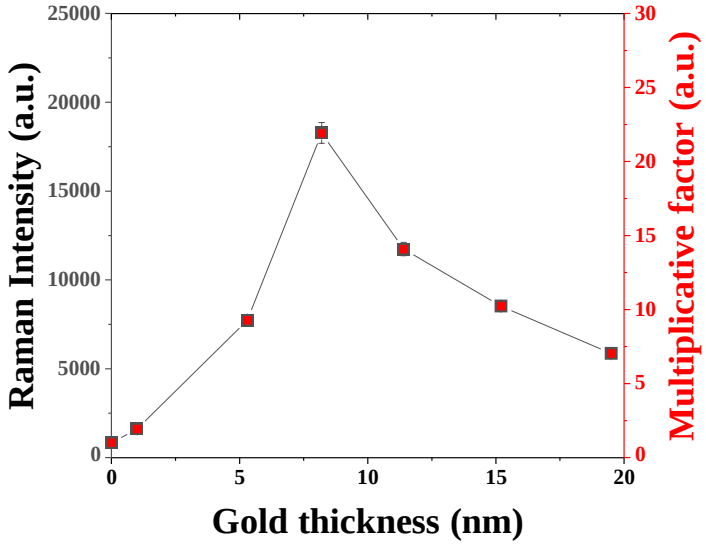

Figure 6. Average Raman intensity as function of the deposited gold layer thickness. The multiplication factors are calculated for each sample with respect to the reference (0s) Au substrate. P = 2 mW; t = 0.5s; λ = 633 nm.

To evaluate the enhancement performance of our optimized substrate, the characteristic Raman band intensity at 1000 cm^{-1} of the typical thiophenol molecule was selected to calculate the analytical enhancement factor (AEF) according to formula (1) [44]:

$$AEF = \frac{I_{SERS}/C_{SERS}}{I_{Ram}/C_{Ram}}$$

Here, I_{SERS} and I_{Ram} are intensities of the characteristic Raman band at 1000 cm^{-1} of thiophenol by SERS and the normal Raman, respectively. C_{SERS} and C_{Ram} are the molar concentrations of 10^{-6} M in the SERS and 10^{-3} M Raman, respectively. The AEF value is then estimated to 5 x 10^4 which is similar to values reported in literature [45–47]. As expected, the AEF value is bounded by the

electromagnetic contribution to SERS determined previously by photoemission microscopy ($< 29^4 = 7 \times 10^5$).

Considering the results presented in Figure 4 and in Figure 6, the hypothesis of a close correlation between the optical responses of the exalted substrate in the near field (PEEM) (without molecules) and in the far field (Raman, with molecules) appears "natural". Note that the polarization of the light is distinct in both experiments (see experimental section). However, the manipulated average quantities are still relevant and comparable as they describe the statistical optical response of a random metal film. To go further, we calculated, for comparison, the intensity histograms of the PEEM and Raman signals for each Au deposit. First, a pixel binning procedure was applied to the high-resolution 3PPE PEEM images to obtain equivalent pixels of the size of the Raman step. In more detail, 10 x 10 µm² PEEM fields of view were binned to normalized maps of 10 x 10 pixels to match the RAMAN measurement step of 1 µm. Signal intensity histograms were then computed. As an example, Figure S3 presents the distribution of PEEM and Raman intensities for 8.2 and 19.5 nm coated samples. For both data sets, the full widths at half maximum (FWHM) of the intensity distributions are larger for 8.2 nm than for 19.5 nm. Ratios of the average intensities for these two exposure times give approximatively $I_{PEEM}(8.2nm)/I_{PEEM}(19.5nm) = 6.25$ for R_{PEEM} and $I_{Raman}(8.2nm)/I_{Raman}(19.5nm) = 3.9$ for R_{Raman}. Let us remind that, for a Au surface, the PEEM signal intensity scales with the amplitude of the incident electric field as E^6 whereas the Raman intensity is proportional to E^4 [48]. Thus, the conversion of R_{PEEM} to a E^4 field scaling leads to a value of 3.4 in close agreement to the one found for Raman. Again, such a result reflects a clear correlation between experimental signal intensities recorded in PEEM and Raman. Using the same analysis procedure (PEEM data binning to a matrix of 10 pixels by 10 pixels) we studied the

full series of substrates. Figure 7 (insets) shows the evolution of the PEEM and Raman intensity distributions as a function of treatment time. It can be clearly observed that the higher the intensity, the larger the distribution. The substrate with an additional gold layer of about 8.2 nm remains the one which produces the highest PEEM and Raman intensities. Experimental data sets evolve consistently in terms of relative maxima and FWHMs. Let us remind that it is the process of binning that leads to the PEEM distribution presented in Figure 7; the near-field optical response of our

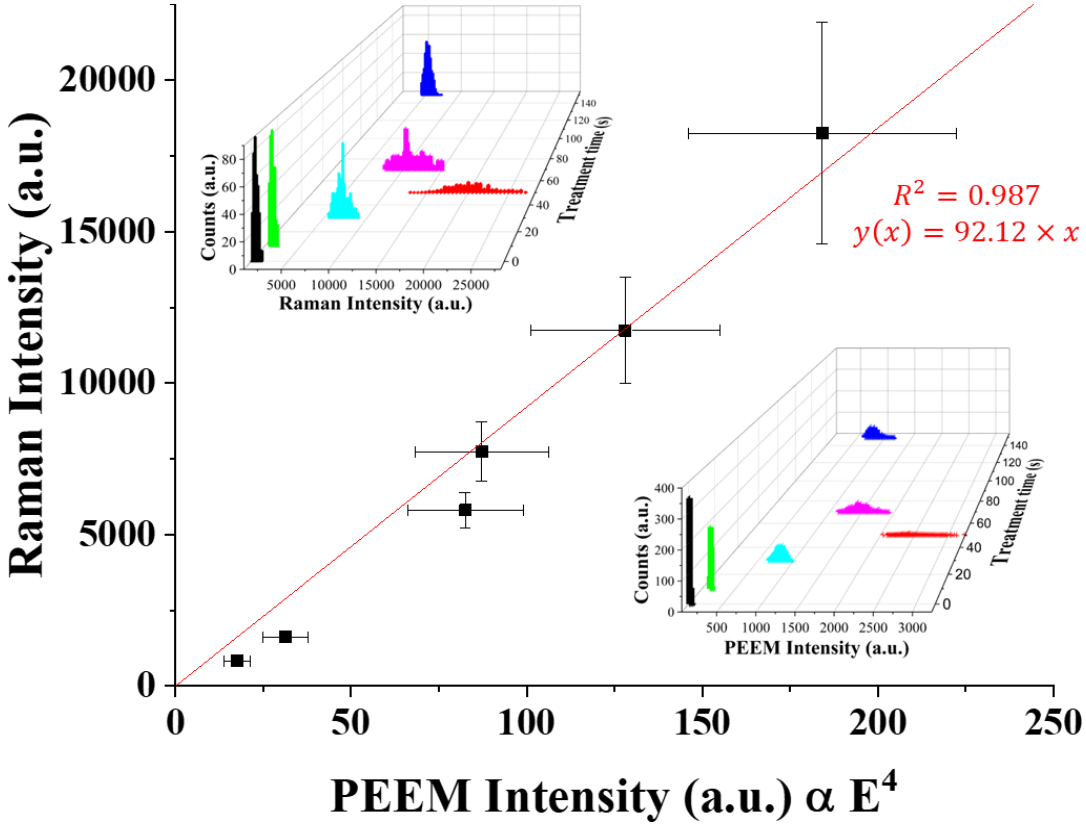

Figure 7. Averaged Raman intensity versus the averaged PEEM intensity. The two data sets show a clear linear correlation. Insets: Raman and PEEM intensity distributions function of treatment time, respectively top and bottom.

random metallic film has, as expected [33], a Log Normal distribution (Figure S4).

Moreover, by taking advantage of these binned PEEM data, one can plot the averaged Raman intensity versus the averaged PEEM intensity. As the PEEM signal intensity is proportional to the amplitude of the incident electric field as E^6 whereas the Raman intensity is proportional to E^4, a

nonlinear evolution is expected. Figure 7 shows that the relationship between both experimental data can reasonably be well approximated. If the PEEM intensities are modified to a E^4 field scaling, a linear regression is clearly obtained and the high value of the regression coefficient R^2 (0.987) confirms the proportionality between the Raman and PEEM intensities. A similar result can also be found (Figure S5) if we plot directly the averaged Raman intensity versus the averaged PEEM hot spots intensity per µm² presented previously in Figure 4, thus confirming that the binning approach does not affect the analysis of the correlations that exist between the near and far field optical responses.

Finally, to test the performance of our optimized sample (8.2nm), SERS measurements have been performed from solutions of thiophenol (TP), Crystal Violet (CV) and rhodamine B (RhB) molecules at 10^{-8} M (trace level). The experimental conditions are identical for all the samples; the surfaces were immersed in the solutions for 10 minutes, rinsed with ethanol and water, air-dried and then analyzed under a microscope. 400 spectra were recorded from a 20 x 20 µm² area mapping with a 2D map step size of 1 µm and then an average spectrum is calculated. Figure 8 shows the Raman spectra of thiophenol, Violet Crystal and rhodamine B at 10^{-6} and 10^{-8} M. The characteristic vibrational modes of the analytes can be easily identified with well-defined bands, even at 10^{-8} M and for molecules that do not graft to the gold surface. Let us also note that no additional band (possible environmental molecules captured after elaboration or during the analysis) is juxtaposed to the Raman spectrum of the molecule to detect as can happen with some commercial substrates with pronounced 3D architectures[49]. This is an essential and indispensable specificity to be verified on any support which would be used for applications as a sensor of molecules in the trace state. According to the high spectral quality (high signal to noise ratio of spectra recorded in less than 7

min), we demonstrated that our optimized SERS-active substrates have sufficient strong performance and sensitivity for molecular detection.

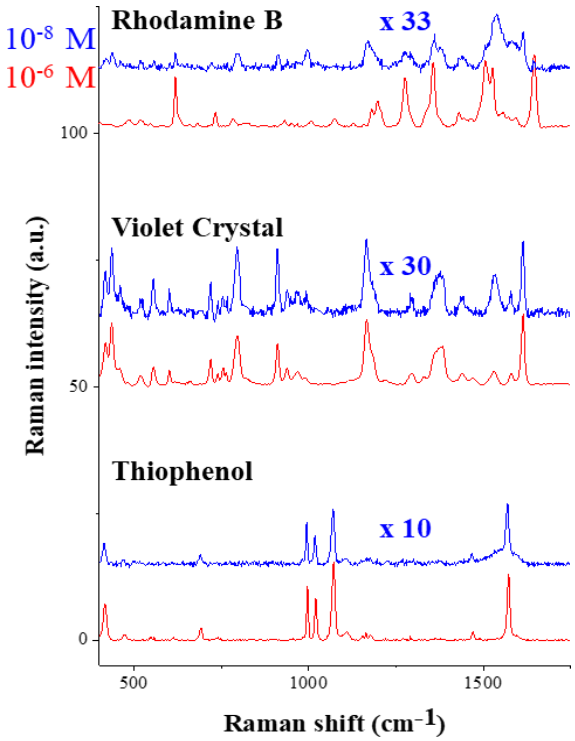

Figure 8. Averaged Raman spectra calculated from the recorded maps of rhodamine B, Violet Crystal and thiophenol at 10^{-6} (red curve) and 10^{-8} M (blue curve), respectively. P = 1 mW; t = 1; λ = 633 nm. The Raman spectra are vertically shifted and amplified by various factors (x33, x30 and x10) for clarity.

In summary, we have demonstrated that the non-invasive optical near field (PEEM) and far field (Raman) responses of Au random surfaces are closely correlated. In particular, we have shown that the intrinsic performance of SERS substrates depends quantitatively on both the surface density and the intensity distribution of hot spots measured by photoemitted electrons. In addition, thiophenol molecule detection at 10^{-6} M by Raman imaging on optimized nanorough gold substrates proves that simple thermal evaporation technique can be used to prepare large area homogeneous and efficient SERS-active substrates with an excellent spatial reproducibility. We

believe therefore the reported results will be of interest to many research groups wishing to develop their own SERS substrates for various applications including detection and identification of trace and bio or molecular sensing since such substrate can detect molecules from 10^{-6} and 10^{-8} M.

EXPERIMENTAL SECTION

Substrate fabrication. Samples were prepared by cleaning a silicon wafer (Ø = 10cm, BT Electronics, Intrinsic-SSP, thickness = 500-550 µm) in HCl/MeOH (1:1) solution, then deionized water and dried under normal air conditions. The cleaned Si substrate was then placed into a thermal evaporator (Plassys ME300, France) and a 100 nm thick gold layer (atom flux controlled by a quartz microbalance system) was deposited with a rate of 0.1 nm/s at a pressure of 5.10^{-6} mbar (Scheme 1). Our reference substrate made of 100 nm of gold on silicon wafer has been chosen to avoid any Raman signals from the silicon wafer (first and second order at 520 cm^{-1} and 1000 cm^{-1} respectively) during SERS measurements. The silicon/gold reference substrate was then cut into small pieces of about 8 x 8 mm^2. On each small piece, an additional gold deposition was made by thermal evaporation with different exposure times (1-150 s) in order to study the relative influence of the surface topography on hot spot density and thus on SERS intensity. The fabrication process is summarized in Scheme 1.

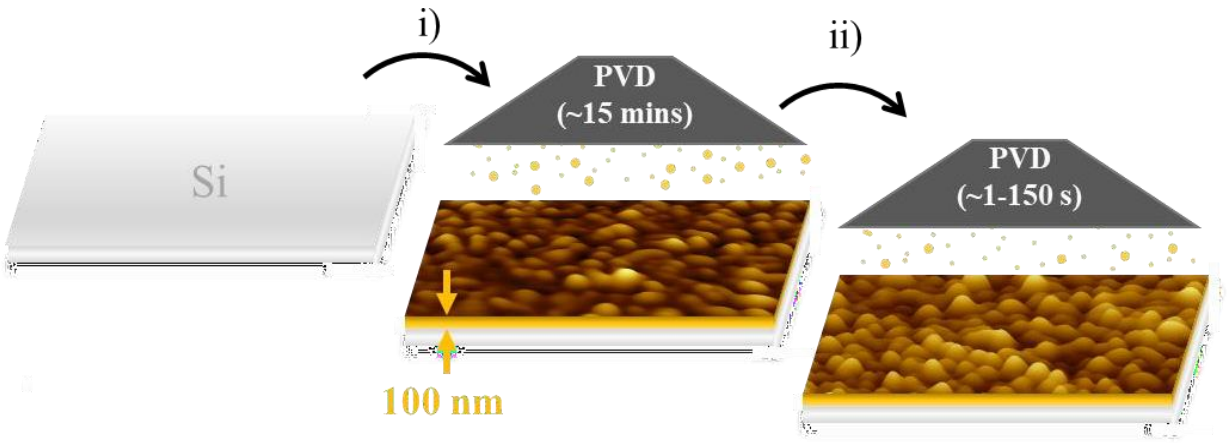

Scheme 1. Schematic representation of the fabrication of the SERS substrates. Two steps preparation method: (i) Deposit of 100 nm of gold by PVD on silicon wafer and (ii) additional gold depositions of increasing thickness (0 to 19.5 nm).

Surface functionalization. Thiophenol (97%, ACROS Organics), Crystal violet (ACS reagent, ≥90% anhydrous basis, Sigma-Aldrich) and Rhodamine B (Sigma-Aldrich) were each diluted with ethanol (99.8%, Sigma-Aldrich) to obtain a 10^{-6} M and 10^{-8} M of respective solutions. The different substrates (gold-treated silicon/gold wafer) were immersed in 2 ml of solutions for 10 minutes, then rinsed into ethanol (30 s) and ultrapure water (30s) to remove non-specific binding molecules. The functionalized substrates were then studied by Raman imaging without any additional cleaning.

Instrumentation

Scanning Electron Microscopy (SEM). SEM images were recorded using a ZEISS SUPRA 55 SAPPHIRE (Carl Zeiss, Jena, Germany) scanning electron microscope under a dynamic high vacuum of the order of 8.10^{-6} Pa. The SEM is equipped with a field emission electron gun (FEG). The measurements were done at 3 kV.

Statistical analysis of surface morphology. To calculate the average grain size from the SEM images we used the Interface Distribution Function (IDF) method.[34] This function is the second derivative of the height autocorrelation function (ACF) which can be calculated from any 2D images. It represents the probability distribution of finding two interfaces at a distance r. The first negative minimum of this function corresponds to the long period of the surface and the first positive maxima to the grain sizes and the inter-grain distances. For the calculation of IDF, radial-ACF function was extracted from the SEM images using Gwyddion freeware. Origin® software was used to calculate the IDF function from the radial-ACF.

Atomic force microscopy (AFM). Film-thickness measurements were carried out using an Agilent 5500 AFM in intermittent-contact mode. To determine the thickness of the additional gold layer, bare silicon wafers were systematically added to the sample holder during the gold deposition. The gold layer was then scratched to reveal the underlying silicon substrate and an AFM image of the scratched region was performed. Film thickness can then be calculated from the distance between the two maxima of the height distribution function.

PEEM Microscopy. An Elmitec SPELEEM III photoemission electron (PEEM) microscope working under UHV pressure was used. PEEM fields of view vary from 1 to 120 µm, with a spatial resolution better than 20 nm. Surface illumination was carried out at the visible wavelength of 633 nm to match the Raman excitation wavelength. A Ti:Al_2O_3 pulsed laser source (Chameleon Ultra II Coherent Inc. 150 fs pulse duration) was used to pump an optical parametric oscillator (Mira OPO APE GmbH) delivering 295 fs light pulse at 633 nm. Polarisation is transverse magnetic (P). Laser irradiance is in the range 1-3 GW/cm². The angle of incidence is fixed to 13° (grazing incidence).

PEEM image processing. Hot pots are counted by image processing. Specifically, PEEM images are cross-correlated with a representative signature of the hot spots (pattern recognition). Thresholding is then applied to the correlation product to extract the positions of the hot spots within the image. Knowing the position of hot spots in an image gives access to their respective maximum intensities and allows the construction of histograms. Image processing is performed using a homemade software (ImaGo L. Douillard CEA IRAMIS SPEC). Gwyddion was also used for additional data processing.

Raman analysis. Raman measurements were performed using a Witec Alpha 300R confocal Raman spectrometer. The spectrometer is equipped with both a 633 nm (He-Ne laser), and 600 tr/mm grating which results in 2 cm^{-1} spectral resolution. The Raman spectra were recorded in air using a Zeiss x100 magnification objective (N.A. = 0.9), spot size around 1 µm, in backscattering configuration. The laser power at the sample and time integration were fixed respectively at P = 2 mW and 0.5s to avoid unintended surface modification or degradation. For each condition, 4 substrates were systematically elaborated and 3 different area mappings (20 x 20 $µm^2$ with a X and Y step 1 µm) were acquired on each substrate. Data processing was done using the Witec Project Five software (version 5.1) including the cosmic ray removal correction function and a shape function for the background subtraction.

ASSOCIATED CONTENT

Supporting Information.

AUTHOR INFORMATION

† Institut des Molécules et Matériaux du Mans UMR CNRS 6283, Le Mans Université, Le Mans, France

‡ Université Paris-Saclay, CEA SPEC, CNRS 3680, 91190 Gif-sur-Yvette, France

Corresponding Author

*E-mail: Jean-Francois.Bardeau@univ-lemans.fr

Author Contributions

Pierre Taugeron: Methodology, Substrates elaborations, Formal analysis, PEEM and Raman Investigations, Writing – original draft, Writing – review & editing. **Meryem Rahmani**: Substrates elaborations, Raman Investigations, Formal analysis. **Nicolas Delorme**: Methodology, Formal analysis, Statistical analysis, Writing – review & editing. **M. Faure** : PEEM investigation, data analysis. **Ludovic Douillard**: Methodology, PEEM Investigations, Formal analysis, Writing – review & editing. **Jean-François Bardeau**: Conceptualization, Methodology, Formal analysis, Investigation, Writing – original draft, Writing – review & editing, Funding acquisition, Supervision.

Funding Sources

We thank both the AGENCE NATIONALE DE LA RECHERCHE and l'AGENCE FRANCAISE POUR LA BIODIVERSITE (AFB) for having sponsored this study in the frame of the HYDRAE project - ANR – AAP 2019 - CE34 [Grant Number: 192393] and the DIPP-SUF project - [AFB - Grant Number: 197176].

Notes

The authors declare that they have no known competing financial interests or personal relationships that could have appeared to influence the work reported in this paper.

ACKNOWLEDGMENT

We would like to thank Stephanie Gacoin from CRISMAT-ENSICAEN, UMR CNRS 6508 (Caen University, France) for providing the SEM images. CEA authors thank Mansour Achaour and Dominique Martinotti from CEA SPEC for their valuable contributions in PEEM data acquisition.

REFERENCES

(1) Fleischmann, M.; Hendra, P. J.; McQuillan, A. J. Raman Spectra of Pyridine Adsorbed at a Silver Electrode. *Chemical Physics Letters* **1974**, *26* (2), 163–166. https://doi.org/10.1016/0009-2614(74)85388-1.

(2) Jeanmaire, D. L.; Van Duyne, R. P. Surface Raman Spectroelectrochemistry: Part I. Heterocyclic, Aromatic, and Aliphatic Amines Adsorbed on the Anodized Silver Electrode. *Journal of Electroanalytical Chemistry and Interfacial Electrochemistry* **1977**, *84* (1), 1–20. https://doi.org/10.1016/S0022-0728(77)80224-6.

(3) Otto, A. Excitation of Nonradiative Surface Plasma Waves in Silver by the Method of Frustrated Total Reflection. *Z. Physik* **1968**, *216* (4), 398–410. https://doi.org/10.1007/BF01391532.

(4) Otto, A. Surface-Enhanced Raman Scattering: "Classical" and "Chemical" Origins. **1984**. https://doi.org/10.1007/3-540-11942-6_24.

(5) Campion, A.; Kambhampati, P. Surface-Enhanced Raman Scattering. *Chem. Soc. Rev.* **1998**, *27* (4), 241–250. https://doi.org/10.1039/A827241Z.

(6) Kim, J.; Jang, Y.; Kim, N.-J.; Kim, H.; Yi, G.-C.; Shin, Y.; Kim, M. H.; Yoon, S. Study of Chemical Enhancement Mechanism in Non-Plasmonic Surface Enhanced Raman Spectroscopy (SERS). *Front. Chem.* **2019**, *7*, 582. https://doi.org/10.3389/fchem.2019.00582.

(7) Ding, S.-Y.; You, E.-M.; Tian, Z.-Q.; Moskovits, M. Electromagnetic Theories of Surface-Enhanced Raman Spectroscopy. *Chem. Soc. Rev.* **2017**, *46* (13), 4042–4076. https://doi.org/10.1039/C7CS00238F.

(8) Nieuwoudt, M. K.; Martin, J. W.; Oosterbeek, R. N.; Novikova, N. I.; Wang, X.; Malmström, J.; Williams, D. E.; Simpson, M. C. Gold-Sputtered Blu-Ray Discs: Simple and Inexpensive SERS Substrates for Sensitive Detection of Melamine. *Anal Bioanal Chem* **2016**, *408* (16), 4403–4411. https://doi.org/10.1007/s00216-016-9545-5.

(9) Kneipp, K.; Wang, Y.; Kneipp, H.; Perelman, L. T.; Itzkan, I.; Dasari, R. R.; Feld, M. S. Single Molecule Detection Using Surface-Enhanced Raman Scattering (SERS). *Phys. Rev. Lett.* **1997**, *78* (9), 1667–1670. https://doi.org/10.1103/PhysRevLett.78.1667.

(10) Yoon, H.; Suh, J. S. Universal Substrates Based on Ag Colloidal Particles for Routine Surface-Enhanced Raman Scattering Spectral Measurements. *RSC Adv.* **2017**, *7* (46), 28573–28579. https://doi.org/10.1039/C7RA04871H.

(11) Abalde-Cela, S.; Aldeanueva-Potel, P.; Mateo-Mateo, C.; Rodríguez-Lorenzo, L.; Alvarez-Puebla, R. A.; Liz-Marzán, L. M. Surface-Enhanced Raman Scattering Biomedical Applications of Plasmonic Colloidal Particles. *J. R. Soc. Interface.* **2010**, *7* (suppl_4). https://doi.org/10.1098/rsif.2010.0125.focus.

(12) Vieu, C.; Carcenac, F.; Pépin, A.; Chen, Y.; Mejias, M.; Lebib, A.; Manin-Ferlazzo, L.; Couraud, L.; Launois, H. Electron Beam Lithography: Resolution Limits and Applications. *Applied Surface Science* **2000**, *164*, 111–117. https://doi.org/10.1016/S0169-4332(00)00352-4.

(13) Abu Hatab, N. A.; Oran, J. M.; Sepaniak, M. J. Surface-Enhanced Raman Spectroscopy Substrates Created via Electron Beam Lithography and Nanotransfer Printing. *ACS Nano* **2008**, *2* (2), 377–385. https://doi.org/10.1021/nn7003487.

(14) Yue, W.; Wang, Z.; Yang, Y.; Chen, L.; Syed, A.; Wong, K.; Wang, X. Electron-Beam Lithography of Gold Nanostructures for Surface-Enhanced Raman Scattering. *J. Micromech. Microeng.* **2012**, 10.

(15) Wu, T.; Lin, Y.-W. Surface-Enhanced Raman Scattering Active Gold Nanoparticle/Nanohole Arrays Fabricated through Electron Beam Lithography. *Applied Surface Science* **2018**, *435*, 1143–1149. https://doi.org/10.1016/j.apsusc.2017.11.213.

(16) Dhawan, A.; Gerhold, M.; Vo-Dinh, T. Theoretical Simulation and Focused Ion Beam Fabrication of Gold Nanostructures for Surface-Enhanced Raman Scattering (SERS). *Nanobiotechnol* **2007**, *3* (3–4), 164–171. https://doi.org/10.1007/s12030-008-9017-x.

(17) Sivashanmugan, K.; Liao, J.-D.; You, J.-W.; Wu, C.-L. Focused-Ion-Beam-Fabricated Au/Ag Multilayered Nanorod Array as SERS-Active Substrate for Virus Strain Detection. *Sensors and Actuators B: Chemical* **2013**, *181*, 361–367. https://doi.org/10.1016/j.snb.2013.01.035.

(18) Dubkov, S. V.; Savitskiy, A. I.; Trifonov, A. Y.; Yeritsyan, G. S.; Shaman, Yu. P.; Kitsyuk, E. P.; Tarasov, A.; Shtyka, O.; Ciesielski, R.; Gromov, D. G. SERS in Red Spectrum Region through Array of Ag–Cu Composite Nanoparticles Formed by Vacuum-Thermal Evaporation. *Optical Materials: X* **2020**, *7*, 100055. https://doi.org/10.1016/j.omx.2020.100055.

(19) Oh, M.-K. Morphological and SERS Properties of Silver Nanorod Array Films Fabricated by Oblique Thermal Evaporation at Various Substrate Temperatures. **2015**, 9.

(20) Gromov, D. G.; Dubkov, S. V.; Savitskiy, A. I.; Shaman, Yu. P.; Polokhin, A. A.; Belogorokhov, I. A.; Trifonov, A. Yu. Optimization of Nanostructures Based on Au, Ag, Au Ag Nanoparticles Formed by Thermal Evaporation in Vacuum for SERS Applications. *Applied Surface Science* **2019**, *489*, 701–707. https://doi.org/10.1016/j.apsusc.2019.05.286.

(21) Huang, Z.; Meng, G.; Huang, Q.; Yang, Y.; Zhu, C.; Tang, C. Improved SERS Performance from Au Nanopillar Arrays by Abridging the Pillar Tip Spacing by Ag Sputtering. *Adv. Mater.* **2010**, *22* (37), 4136–4139. https://doi.org/10.1002/adma.201001179.

(22) Dornhaus, R.; Benner, R. E.; Chang, R. K.; Chabay, I. Surface Plasmon Contribution to SERS. *Surface Science* **1980**, *101* (1), 367–373. https://doi.org/10.1016/0039-6028(80)90632-9.

(23) Merlen, A.; Gadenne, V.; Romann, J.; Chevallier, V.; Patrone, L.; Valmalette, J. C. Surface Enhanced Raman Spectroscopy of Organic Molecules Deposited on Gold Sputtered Substrates. *Nanotechnology* **2009**, *20* (21), 215705. https://doi.org/10.1088/0957-4484/20/21/215705.

(24) Maya, L.; Vallet, C. E.; Lee, Y. H. Sputtered Gold Films for Surface-Enhanced Raman Scattering. *Journal of Vacuum Science & Technology A: Vacuum, Surfaces, and Films* **1997**, *15* (2), 238–242. https://doi.org/10.1116/1.580518.

(25) Yu, X.; Duxbury, P. M.; Jeffers, G.; Dubson, M. A. Coalescence and Percolation in Thin Metal Films. *Phys. Rev. B* **1991**, *44* (23), 13163–13166. https://doi.org/10.1103/PhysRevB.44.13163.

(26) Zhang, C.; Ji, C.; Park, Y.; Guo, L. J. Thin-Metal-Film-Based Transparent Conductors: Material Preparation, Optical Design, and Device Applications. *Adv. Optical Mater.* **2021**, *9* (3), 2001298. https://doi.org/10.1002/adom.202001298.

(27) Noh, J.; Ito, E.; Hara, M. Self-Assembled Monolayers of Benzenethiol and Benzenemethanethiol on Au(111): Influence of an Alkyl Spacer on the Structure and Thermal Desorption Behavior. *Journal of Colloid and Interface Science* **2010**, *342* (2), 513–517. https://doi.org/10.1016/j.jcis.2009.10.076.

(28) Douillard, L.; Charra, F.; Korczak, Z.; Bachelot, R.; Kostcheev, S.; Lerondel, G.; Adam, P.-M.; Royer, P. Short Range Plasmon Resonators Probed by Photoemission Electron Microscopy. *Nano Lett.* **2008**, *8* (3), 935–940. https://doi.org/10.1021/nl080053v.

(29) Awada, C.; Barbillon, G.; Charra, F.; Douillard, L.; Greffet, J.-J. Experimental Study of Hot Spots in Gold/Glass Nanocomposite Films by Photoemission Electron Microscopy. *Phys. Rev. B* **2012**, *85* (4), 045438. https://doi.org/10.1103/PhysRevB.85.045438.

(30) Awada, C.; Plathier, J.; Dab, C.; Charra, F.; Douillard, L.; Ruediger, A. High Resolution Scanning near Field Mapping of Enhancement on SERS Substrates: Comparison with Photoemission Electron Microscopy. *Phys. Chem. Chem. Phys.* **2016**, *18* (14), 9405–9411. https://doi.org/10.1039/C5CP08015K.

(31) Liu, Z. H.; Brown, N. M. D.; McKinley, A. Evaluation of the Growth Behaviour of Gold Film Surfaces Evaporation-Deposited on Mica under Different Conditions. *J. Phys.: Condens. Matter* **1997**, *9* (1), 59–71. https://doi.org/10.1088/0953-8984/9/1/009.

(32) Barnes, M. C.; Kim, D.-Y.; Ahn, H. S.; Lee, C. O.; Hwang, N. M. Deposition Mechanism of Gold by Thermal Evaporation: Approach by Charged Cluster Model. *Journal of Crystal Growth* **2000**, *213* (1–2), 83–92. https://doi.org/10.1016/S0022-0248(00)00359-6.

(33) Zhang, S.; Berguiga, L.; Elezgaray, J.; Roland, T.; Faivre-Moskalenko, C.; Argoul, F. Surface Plasmon Resonance Characterization of Thermally Evaporated Thin Gold Films. *Surface Science* **2007**, *601*, 5445–5458. https://doi.org/10.1016/j.susc.2007.09.014.
(34) Siniscalco, D.; Edely, M.; Bardeau, J.-F.; Delorme, N. Statistical Analysis of Mounded Surfaces: Application to the Evolution of Ultrathin Gold Film Morphology with Deposition Temperature. *Langmuir* **2013**, *29* (2), 717–726. https://doi.org/10.1021/la304621k.
(35) Malureanu, R.; Lavrinenko, A. Ultra-Thin Films for Plasmonics: A Technology Overview. *Nanotechnology Reviews* **2015**, *4* (3), 259–275. https://doi.org/10.1515/ntrev-2015-0021.
(36) Gaspar, D.; Pimentel, A. C.; Mateus, T.; Leitão, J. P.; Soares, J.; Falcão, B. P.; Araújo, A.; Vicente, A.; Filonovich, S. A.; Aguas, H.; Martins, R.; Ferreira, I. Influence of the Layer Thickness in Plasmonic Gold Nanoparticles Produced by Thermal Evaporation. *Sci Rep* **2013**, *3*, 1469. https://doi.org/10.1038/srep01469.
(37) Ducourtieux, S.; Podolskiy, V. A.; Grésillon, S.; Buil, S.; Berini, B.; Gadenne, P.; Boccara, A. C.; Rivoal, J. C.; Bragg, W. D.; Banerjee, K.; Safonov, V. P.; Drachev, V. P.; Ying, Z. C.; Sarychev, A. K.; Shalaev, V. M. Near-Field Optical Studies of Semicontinuous Metal Films. *Phys. Rev. B* **2001**, *64* (16), 165403. https://doi.org/10.1103/PhysRevB.64.165403.
(38) Mertens, S.; Moore, C. Continuum Percolation Thresholds in Two Dimensions. *Phys. Rev. E* **2012**, *86* (6), 061109. https://doi.org/10.1103/PhysRevE.86.061109.
(39) Quintanilla, J. A.; Ziff, R. M. Asymmetry in the Percolation Thresholds of Fully Penetrable Disks with Two Different Radii. *Phys. Rev. E* **2007**, *76* (5), 051115. https://doi.org/10.1103/PhysRevE.76.051115.
(40) Sinthiptharakoon, K.; Sapcharoenkun, C.; Nuntawong, N.; Duong, B.; Wutikhun, T.; Treetong, A.; Meemuk, B.; Kasamechonchung, P.; Klamchuen, A. Conductive Scanning Probe Microscopy of the Semicontinuous Gold Film and Its SERS Enhancement toward Two-Step Photo-Induced Charge Transfer and Effect of the Supportive Layer. *Applied Surface Science* **2018**, *441*, 364–371. https://doi.org/10.1016/j.apsusc.2018.01.269.
(41) Novikov, S. M.; Beermann, J.; Frydendahl, C.; Stenger, N.; Coello, V.; Mortensen, N. A.; Bozhevolnyi, S. I. Enhancement of Two-Photon Photoluminescence and SERS for Low-Coverage Gold Films. *Opt. Express, OE* **2016**, *24* (15), 16743–16751. https://doi.org/10.1364/OE.24.016743.
(42) Zhu, W.; Crozier, K. B. Quantum Mechanical Limit to Plasmonic Enhancement as Observed by Surface-Enhanced Raman Scattering. *Nat Commun* **2014**, *5* (1), 5228. https://doi.org/10.1038/ncomms6228.
(43) Rácz, P.; Pápa, Z.; Márton, I.; Budai, J.; Wróbel, P.; Stefaniuk, T.; Prietl, C.; Krenn, J. R.; Dombi, P. Measurement of Nanoplasmonic Field Enhancement with Ultrafast Photoemission. *Nano Lett.* **2017**, *17* (2), 1181–1186. https://doi.org/10.1021/acs.nanolett.6b04893.
(44) Le Ru, E. C.; Blackie, E.; Meyer, M.; Etchegoin, P. G. Surface Enhanced Raman Scattering Enhancement Factors: A Comprehensive Study. *J. Phys. Chem. C* **2007**, *111* (37), 13794–13803. https://doi.org/10.1021/jp0687908.
(45) Pavel, I. E.; Alnajjar, K. S.; Monahan, J. L.; Stahler, A.; Hunter, N. E.; Weaver, K. M.; Baker, J. D.; Meyerhoefer, A. J.; Dolson, D. A. Estimating the Analytical and Surface Enhancement Factors in Surface-Enhanced Raman Scattering (SERS): A Novel Physical Chemistry and Nanotechnology Laboratory Experiment. *J. Chem. Educ.* **2012**, *89* (2), 286–290. https://doi.org/10.1021/ed200156n.
(46) Cialla, D.; März, A.; Böhme, R.; Theil, F.; Weber, K.; Schmitt, M.; Popp, J. Surface-Enhanced Raman Spectroscopy (SERS): Progress and Trends. *Anal Bioanal Chem* **2012**, *403* (1), 27–54. https://doi.org/10.1007/s00216-011-5631-x.
(47) Kadir, M.; Nemkayeva, R.; Baigarinova, G.; Alpysbayeva, B.; Assembayeva, A.; Smirnov, V. SERS-Active Substrates Based on Ag-Coated TiO2 Nanotubes and Nanograss. *Physica E: Low-dimensional Systems and Nanostructures* **2023**, *145*, 115499. https://doi.org/10.1016/j.physe.2022.115499.

(48) Ru, E.; Etchegoin, P. Principles of Surface-Enhanced Raman Spectroscopy: And Related Plasmonic Effects; 2008.

(49) Rahmani, M; Taugeron, P; Rousseau, A.; Delorme, N; Douillard, L.; Duponchel, L; Bardeau, J.-F. Highlight on commercial SERS substrates and optimized nanorough large-area SERS-based sensors: A Raman study. Submitted.